Improving the analysis and inversion of multimode Rayleigh-wave dispersion by using group-delay time information observed on arrays of high-frequency sensors

Zacharie Duputel[1], Michel Cara[1], Luis Rivera[1], and Georges Herquel[1]

ABSTRACT

Near-surface shear-velocity structure can be inferred from multimode dispersion data. Several methods have been developed to isolate the different modes from seismic signals observed on linear arrays of sensors. Most techniques analyze the wavefield through a frequency-wavenumber (f-k) transform, paying little attention to group-delay-time information. Moreover, classical analyses are generally restricted to fundamental-mode dispersion, limiting the resolution power at depth. We have overcome the limitations of classical f-k analysis by using a wavefield representation in the group-velocity/phase-velocity (U-c) domain. We have then set up a nonlinear inversion procedure, easily tractable on a common field computer, to constrain the 1D vertical profile of shear velocities. Applications to synthetic data and to a set of actual records show that U-c diagrams greatly help to separate dispersion information between different modes, even when they are not detectable on usual f-k diagrams. Tests on synthetic and actual data confirm that the inversion procedure quickly converges to the expected model.

INTRODUCTION

In the late 1980s, multichannel analysis of surface waves (MASW) became a popular technique to explore near-surface shear-wave velocity structures (Song et al., 1989; Park et al., 1999). Applications cover geotechnical investigations, seismic site response assessment in earthquake hazard studies, and static seismic corrections in shear-wave profiling (e.g., Mari, 1984).

MASW is based on a frequency-wavenumber (f-k) transform of the seismic signal generated by a controlled source and recorded on a linear array of sensors. This f-k analysis is equivalent to the slow-ness-frequency (p-f) transform that can be obtained from a slant stack followed by a time Fourier transform (McMechan and Yedlin, 1981). In most MASW applications, observation is restricted to the fundamental-mode Rayleigh waves, and inversion of their dispersion provides a 1D vertical distribution of shear-wave velocity beneath the array of sensors (Xia et al., 1999).

Although higher modes may provide strong additional constraints on vertical shear-wave velocity profiles (Gabriels et al., 1987), their use has been limited to a few investigations. For example, Beaty et al. (2002), Xia et al. (2003), and Feng et al. (2005) show that higher-mode observations enable a greater depth of investigation and increase the depth resolution of inverted shear-wave velocity profiles. Measuring higher-mode dispersion is difficult, mainly because of the coalescing of the energy bands in the f-k domain. Other approaches have then been proposed such as the high-resolution linear Radon transform (Luo et al., 2008) or a different representation of the full wavefield (Forbriger, 2003; O'Neil and Matsuoka, 2005; O'Neil et al., 2008). Here, we propose an alternative method by using a time-f-k analysis technique developed more than 30 years ago in earthquake seismology.

In seismology, higher modes trapped in the crust have been observed for a long time (e.g., Oliver and Ewing, 1957). Retrieving higher-mode dispersion information from f-k analysis seems to have been first suggested in mantle seismology by Kovach (1965). Nolet (1975) and Cara (1976) later developed algorithms based on this idea, adding a time-frequency analysis to classical f-k representation. In doing so, they used the group-delay-time information contained in the records.

In Cara's (1976) algorithm, the signals coming from the different sensors are stacked after applying a time- and phase-shift filter in the frequency domain. At a fixed frequency f_p, the energy density exhibits peaks at group velocity $U_n(f_p)$ and phase velocity $c_n(f_p)$, related to each surface-wave mode n. The series of diagrams plotted at different frequencies f_p then allows the analyst to retrieve the fundamental- and higher-mode dispersion curves. In seismology, this mul-

timode analysis technique has been applied to many sets of surface-wave records over the past 30 years (e.g., Merrer et al. [2007] for a recent application to multimode mantle Rayleigh waves; Cara and Minster [1981] for application to crustal L_g-waves). We show here, by using both synthetic and field data, that our U-c diagram technique can be applied successfully to high-frequency near-surface Rayleigh waves and that high depth resolution can be achieved when inverting the multimode dispersion data.

THE METHOD

U-c diagrams

We assume that the signals recorded on a linear array of sensors represent a discrete spatial sampling of the wavefield. In the wavenumber/angular-frequency domain (k, ω), the relation between the Fourier transform of the records $\hat{S}(k, \omega)$ and the actual wavefield $\hat{W}(k, \omega)$ is

$$\hat{S}(k, \omega) = I(\omega)\hat{W}(k, \omega) \times N(\omega) \times \hat{r}(k). \quad (1)$$

Capital letters here indicate functions in the frequency domain while letters with carets indicate functions in the wavenumber or frequency wavenumber domain. In expression 1, $I(\omega)$ is the instrument transfer function, $N(\omega)$ is the Fourier transform of the time sampling function, and $\hat{r}(k)$ is the so-called array response (e.g., Merrer et al., 2007). The array response $\hat{r}(k)$ is given by

$$\hat{r}(k) = \sum_{n=0}^{N-1} w_n \exp ikx_n, \quad (2)$$

where x_n are the spatial coordinates of station n and w_n is a weight applied to this station.

The value $\hat{r}(k)$ is the main limiting factor of any space-time analysis (wavenumber resolution and spatial aliasing). If we consider unit weights and regularly spaced sensors every Δx over a linear array of length L, the amplitude of the array response becomes

$$|\hat{r}(k)| = L \operatorname{sinc}\frac{kL}{2} \times \frac{1}{\Delta x}\sum_{m=-\infty}^{\infty}\delta\left(k - \frac{2\pi m}{\Delta x}\right), \quad (3)$$

where $\delta(\ )$ is the Dirac delta function. In expression 3, $|\hat{r}(k)|$ is a periodic function of period $2\pi/\Delta x$ with a sinc shape. The array re-

sponse seriously complicates the analysis in f-k diagrams because of the possible misidentification and interferences between the sinc secondary lobes and the higher modes. In classical f-k analysis, no clear method has been proposed to distinguish overtones from these secondary lobes. Taking into account the group-delay-time information here may improve mode identification.

In Cara's (1976) algorithm, multimode signals recorded by an array of N sensors are stacked after applying a narrow-band Gaussian frequency filter and a phase-shift filter to the records to reinforce the individual modes by constructive interference. This leads to the functional

$$G_{\omega_0}(k_0, \omega) = \sum_{n=0}^{N-1} w_n S_{\omega_0}(x_n, \omega)\exp[-iK(\omega)x_n], \quad (4)$$

where $S_{\omega_0}(x_n, \omega)$ is the time Fourier transform of a record $f(x_n, t)$ observed at epicentral distance x_n and filtered around the circular frequency ω_0. The last term in expression 4 is the phase-shift filter, with $K(\omega)$ defined as

$$K(\omega) = k_0 + \frac{\omega - \omega_0}{U_c}, \quad (5)$$

where k_0 is an arbitrary wavenumber and U_c is the central group velocity of the multimode wave packet to be analyzed.

In equation 4, the inverse Fourier transform of $S_{\omega_0}(x_n, \omega)$ corresponds to a superposition of modes centered at times $t_{\omega_0}^m(x_n) = x_n/U_m$, where U_m is the group velocity of the mode m around ω_0. If we assume $k_m(\omega_0) = k_0$ and $dk_m/d\omega|_{\omega_0} \approx U_c^{-1}$, equation 5 becomes the first-order Taylor expansion of the wavenumber $k_m(\omega)$ related to mode m around ω_0. Therefore, if we calculate $G_{\omega_0}(k_0, \omega)$ for several values of k_0, each mode with a wavenumber $k_m(\omega)$ that differs from k_0 around ω_0 will interfere in a noncoherent way. On the other hand, a mode whose wavenumber $k_m(\omega)$ equals k_0 around ω_0 is reinforced by constructive interference. We call the modulus of the inverse Fourier transform $g(k_0, t)$ of $G(k_0, \omega)$ a U-c diagram. It will exhibit peaks at $k_m = \omega_0/c_m$ and $t_m = \bar{x}(U_m^{-1} - U_c^{-1})$ where c_m and U_m are the phase velocity and group velocity of mode m around ω_0 and where $\bar{x} = \Sigma_{n=1}^{N} x_n/N$ (Cara, 1976), the overbar indicating the arithmetic mean over x_n.

We first illustrate this technique with noise-free synthetic Rayleigh-wave displacements corresponding to realistic images of the subsurface (Table 1). Figure 1 displays the Rayleigh waves computed by summing the first six Rayleigh modes excited by a point vertical force located at the surface using Hermann's software package (Herrmann, 2006). Figure 2 compares f-c and U-c diagrams at two fixed frequencies. The f-c diagrams are computed using a p-f transform of the wavefield. The fundamental mode and the first higher mode are clearly visible on the U-c diagrams, whereas the second-higher mode excited by this surficial source is too weak to be observed as a peak on the U-c diagrams.

Figure 3 compares the theoretical and measured dispersions on U-c and f-c diagrams. As expected, the f-c transform is mainly effective in measuring the fundamental-mode phase velocity. In the low-frequency range (i.e., $f < 15$ Hz) because of low wavenumber resolution, interaction between the fundamental and higher modes

Table 1. Tabular models used to compute synthetics. e is the layer thickness, V_P is the compressional wave velocity, V_s is the shear wave velocity, ρ is the density, Q_P and Q_S are the quality factors respectively for P and S waves.

Model	e (m)	V_P (m/s)	V_S (m/s)	ρ (g/cm³)	Q_P	Q_S
Model A	10	692	400	1.7	70	31
	∞	1210	700	1.9	100	44
Model B	3	310	180	1.7	30	13
	10	480	280	1.8	70	31
	∞	780	450	1.9	70	31

makes phase-velocity estimations inaccurate on the *f-c* diagrams (Figure 3, left). Note also that the first overtone associated with model A is too weak to be observed on *f-c* diagrams (Figure 3a, left).

In Figure 3, phase and group velocities observed on *U-c* diagrams are quite close to the theoretical values. The fundamental-mode phase-velocity measurements fit well with the theoretical values, even for frequencies lower than 15 Hz where the classical *f-k* method fails. Regarding model A, we note a phase-velocity misfit that is greater for the first overtone than for the fundamental mode. This is probably because of the low amplitude of the first overtone, which is clearly visible on the *U-c* diagram (Figure 2a, right) but merely detectable on the *f-c* diagram (Figure 2a, left).

However, in Figure 3, the measurement errors on the *U-c* diagrams are larger for group velocity than for phase velocity. One explanation is the lack of time resolution in the time-frequency domain, a common problem in group-velocity analysis. Another explanation is the strong dependency of *U-c* diagrams upon U_c in equation 5; if the group-delay-time analysis helps us separate the different modes, the measured group velocities are less accurate than the phase velocities. In other words, one may say that the *U-c* diagram technique improves the accuracy of the phase-velocity measurements, but that the group-velocity measurements are less accurate.

Parameterization

Here we consider a layered model of the subsurface. Each layer of thickness *e* is characterized by compressional-wave velocity V_P, shear-wave velocity V_S, and density ρ. We can introduce the dimensionless phase-velocity sensitivity kernels

$$K_\gamma(z,f) = \frac{\gamma(z)}{c(f)} \frac{\partial c(f)}{\partial \gamma(z)}, \qquad (6)$$

a logarithmic derivative. Expression 6 is a logarithmic derivative of a given mode phase velocity $c(f)$ at frequency *f* with respect to the parameter $\gamma = V_P, V_S, \rho$ or *e* in the layer at depth *z*.

Figure 4 depicts the sensitivity kernels $K_{V_P}(z)$, $K_{V_S}(z)$, $K_\rho(z)$, and $K_e(z)$ at 28 Hz (mean frequency of measurements on Figure 3a) for model A, concerning the fundamental and first higher mode. When the Poisson's ratio ν is 0.25 or 0.4, the phase velocity mainly de-

Figure 2. The *f-c* and *U-c* diagrams computed from synthetic data, corresponding to (a) model A and (b) model B in Table 1. The vertical dotted black lines on the *f-c* diagrams (left) show the frequencies used to calculate the corresponding *U-c* diagrams (right). The vertical coordinate varies linearly with $1/U$ (time scale) and the horizontal coordinate with $1/c$ (wavenumber scale). The modulus of the array response $|\hat{r}(k)|$ is shown on top of each *U-c* diagram. Black dots indicate the theoretical group and phase-velocity values of the fundamental mode (0) and the first overtones (1-2). Crosses indicate the location of peak maxima for modes 0 and 1.
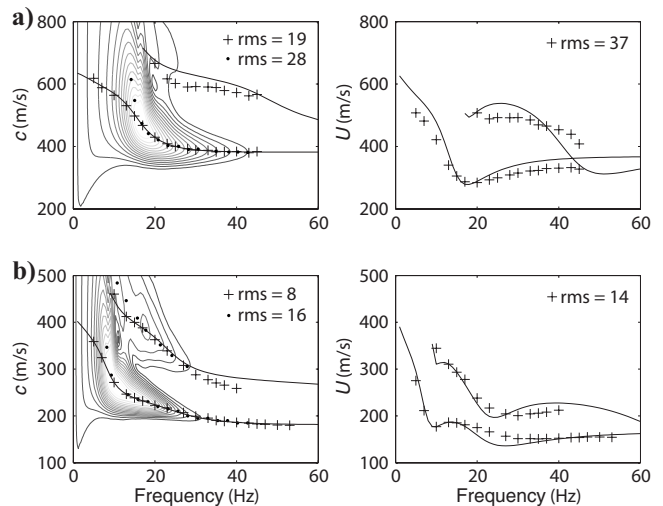
Figure 3. Comparison between measured and theoretical dispersion for (a) model A and (b) model B. On the left are displayed phase velocities *c*, and on the right are group velocities *U*. Solid lines are the theoretical values, black crosses show the values measured on the *U-c* diagrams, and black dots show the phase velocities measured on the *f-c* diagrams. The rms deviation between the theoretical values and measurements are indicated on each graph. The amplitude contour maps of *f-c* diagrams are displayed as a background in the frequency/phase-velocity domain (left).
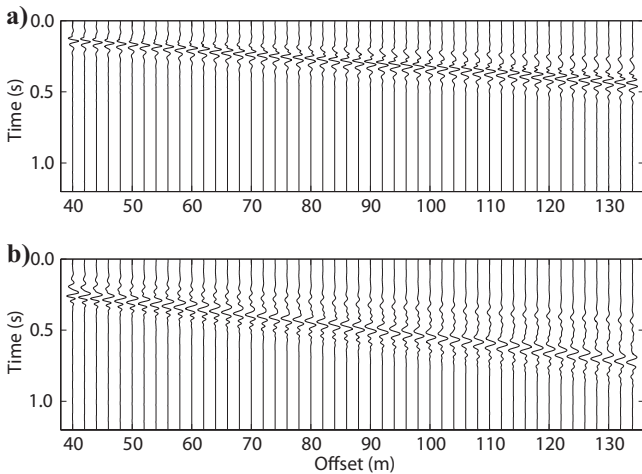
Figure 1. Synthetic seismograms computed by summing the first six Rayleigh modes along a linear array of 48 stations; (a) and (b) correspond to models A and B of Table 1, respectively.
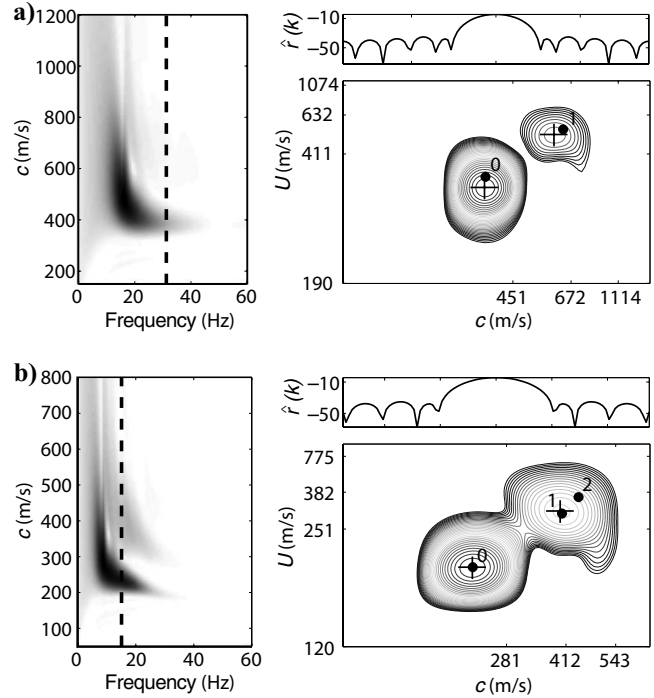
pends on V_S, whereas its dependency on V_P, ρ, and e is very weak for both modes. In the case of a small Poisson's ratio, e.g., 0.1, sensitivity of the fundamental-mode phase velocity with respect to V_P becomes important at very shallow depth ($z < 1.5$ m) but remains negligible for the first-higher mode (Figure 4a). Because surficial layers usually are characterized by a high Poisson's ratio (i.e., high V_P/V_S), we do not consider low values of ν in our application. Note also on Figure 4a and b that the fundamental mode is sensitive to V_S until approximately 10-m depth, whereas the first overtone shows a significant sensitivity to a depth of 23 m. This clearly highlights the importance of inverting the multimode phase velocities to improve the resolution power at large depths (see Xia et al. 2003 or Feng et al. 2005 for detailed sensitivity analyses).

Because V_P and ρ have minimal influence on the phase velocities of the fundamental and higher modes in near-surface Rayleigh waves, Poisson's ratio and density have been fixed to their a priori values in the inversion process. Dispersion data may be more sensitive to the thicknesses of the layers e for large parameter contrasts between two successive thick layers. So instead of inverting for layer thicknesses, we prefer considering many thin layers and starting the inversion from a large series of a priori models. In this way, only V_S, the most sensitive parameter, is inverted in what follows.

Preinversion

We followed two alternative approaches to choose the a priori information on the model parameters $\mathbf{m}_{\text{prior}}$. Each approach can be seen as a preinversion step that precedes the quasi-Newton algorithm described in the next section.

The first approach, often used in subsurface investigations, is somewhat empirical (e.g., Park et al., 1999; Xia et al., 1999; Luo et al., 2007). It provides a smooth, depth-increasing V_S model. We consider a Poisson's solid in a homogeneous half-space to calculate the shear velocity V_S at a depth $z(f)$ according to

$$V_S(z(f)) = \frac{c_0(f)}{0.9194}, \qquad (7)$$

where $c_0(f)$ is the phase-velocity of the fundamental mode at frequency f corresponding to a wavelength $\lambda(f)$ that satisfies $z(f) = \lambda(f)/3$ (e.g., Abbiss, 1981; Socco and Strobbia, 2004). Note that the group-velocity information provided by the U-c diagrams is not taken into account in this approach.

The second approach is strongly nonlinear and is similar to a rough Monte Carlo algorithm. It is based on the exploration of a model library containing several a priori models of the subsurface. This model library is constructed by combining velocities and layer thicknesses commonly encountered in near-surface applications. The database is made of three-layer models, allowing us to consider a large variability in the a priori V_S depth distributions (Table 2). In our model library, velocity increases with depth, but other choices are possible. To ensure a good exploration of the model space, it should be adapted to each specific geologic context. Once the dispersion curves are computed for the whole model library, the computing time is greatly reduced, ensuring the tractability of the inversion process on common portable computers.

Before each inversion, we find the model that minimizes a misfit function $M(\mathbf{m})$, defined as

$$M(\mathbf{m}) = \|\mathbf{c}_{\text{obs}} - \hat{\mathbf{c}}(\mathbf{m})\|^2 + \mu\|\mathbf{U}_{\text{obs}} - \hat{\mathbf{U}}(\mathbf{m})\|^2, \qquad (8)$$
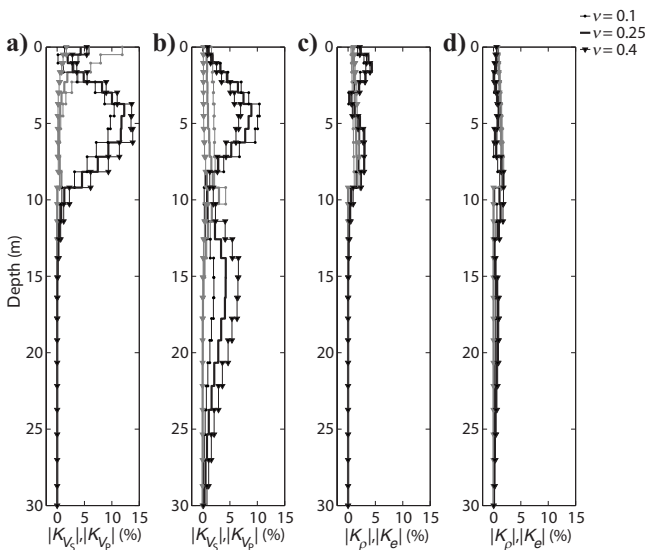
where μ is a constant weighting parameter; $\mathbf{c}_{\text{obs}}$ and $\hat{\mathbf{c}}(\mathbf{m})$ are observed and predicted phase-velocity, respectively; and $\mathbf{U}_{\text{obs}}$ and $\hat{\mathbf{U}}(\mathbf{m})$ are the observed and predicted group velocities. Because the U-c diagrams cannot provide an accurate estimate of the group-velocities, we cannot exclude the possibility that a model which fits the group-velocity data will present strong velocity contrasts that do not reflect the actual subsurface model.

The model selected from this preinversion step will be used as the a priori information $\mathbf{m}_{\text{prior}}$ in a quasi-Newton algorithm. An unrealistic a priori model could compromise the convergence of the inversion, so we put a weighting factor μ in equation 8 to mitigate the possible bias from poor group-velocity estimates. Another possibility would be to include covariance matrices in equation 8 by fixing error values for each mode at each frequency. However, this preinversion step is quite rough, so we prefer to use μ to balance the set of data vectors. Calibration on several synthetic tests led us to set $\mu = 0.5$.

The models resulting from the two preinversion approaches are

Figure 4. Kernel sensitivity of phase velocities at 28 Hz computed for model A (Table 1). The kernels K_{V_P} (gray lines) and K_{V_S} (dark lines) are displayed for (a) the fundamental mode and (b) the first overtone. The kernels K_e (gray lines) and K_ρ (dark lines) are shown for (c) the fundamental mode and (d) the first overtone. Kernel absolute values are presented for different Poisson ratios ν ranging from 0.1 to 0.4.

Table 2. Model library made of two to three layers over the half-space. Extremum values for thickness e and shear velocities V_S are indicated for each layers. In all cases, V_S increases with depth and the half-space V_S is set equal to V_S of the deepest layer. Each model includes at least one interface between a minimal depth of 2.6 m and a maximal depth of 26 m. These are reasonable values knowing the evolution of phase velocities sensitivities with depth (e.g., Figure 4).

Layer	Min e (m)	Max e (m)	Min V_S (m/s)	Max V_S (m/s)
1	2.6	2.6	200	400
2	0.5	23.4	2000	2000
3	0	22.9	2000	2000

displayed as dotted black lines on Figure 5 for models A and B (solid black lines on the same figure). Figure 6 shows the deviations for each layer between the a priori models issued from the preinversion step and the actual ones. Regarding model A, using a model library clearly gives better results than the classical phase-velocity conversion. As shown on Figure 6a, the model extracted from the library fits the exact model very well except at 10-m depth because the interface is not at the right depth in the library models (Figure 5b). The empirical conversion used in the first approach (Figure 5a) provides a smooth V_S profile, leading to an overall greater deviation — particularly for the deepest layer (Figure 6a). This deviation results from the low sensitivity of the fundamental mode at large depth, as seen in Figure 4a-c.

Concerning model B, Figure 5c shows the smoothing effect of the a priori conversion of V_S and the same lack of resolution as before. The lower V_S contrasts of model B as compared to model A permit a rather small deviation from the targeted exact model for the first two layers, but the deepest layer is not resolved at all (Figure 6b). The V_S profile resulting from the model library (Figure 5d) fits the upper and deeper parts of the model reasonably well but is unable to fit the targeted model at 10-m depth, just above the strongly contrasted interface.

In general, the different tests we performed show that the model library provides better results when strong velocity contrasts are involved in the near surface (i.e., $\Delta V_S > 200$ m/s); otherwise, the a priori conversions of phase velocity provide satisfactory V_S profiles.
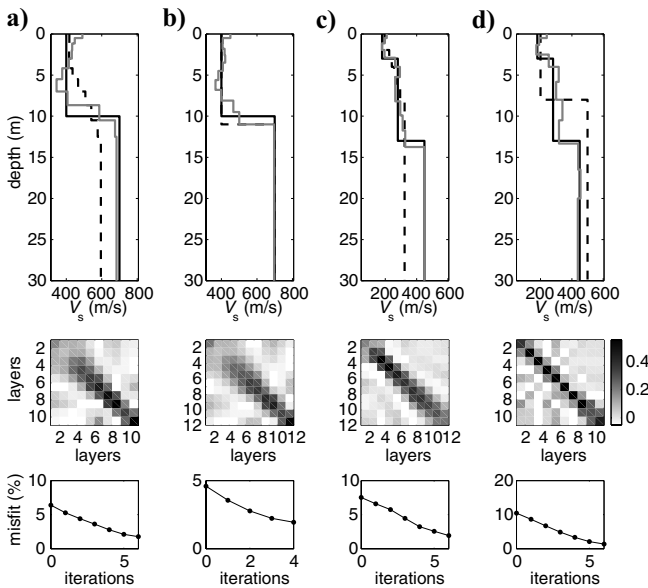
Inversion

Once selected, the preliminary models should fit the data reasonably well (black lines on Figure 7), and explanation of the remaining data misfit can be treated as a weakly nonlinear problem. For this purpose, we use an inversion scheme based on a quasi-Newton algorithm minimizing the phase-velocity misfit function:

$$2S(\mathbf{m}) = \|\mathbf{c}_{\text{obs}} - \hat{\mathbf{c}}(\mathbf{m}_{\text{prior}})\|^2 + \|\,\mathbf{m} - \mathbf{m}_{\text{prior}}\|^2, \quad (9)$$

where $\mathbf{c}_{\text{obs}}$ is the data vector containing the observed phase velocities and $\mathbf{m}_{\text{prior}}$ is a priori model extracted from the preinversion analysis. The layered V_S model at the $n + 1$ iteration is then given by (Tarantola, 2005)

$$\mathbf{m}_{n+1} = \mathbf{m}_n - (\mathbf{G}_n^t \mathbf{C}_\mathbf{D}^{-1} \mathbf{G}_n + \mathbf{C}_\mathbf{M}^{-1})^{-1}[\mathbf{G}_n^t \mathbf{C}_\mathbf{D}^{-1}(\hat{\mathbf{c}}(\mathbf{m}_n) - \mathbf{c}_{\text{obs}})$$
$$+ \mathbf{C}_\mathbf{M}^{-1}(\mathbf{m}_n - \mathbf{m}_{\text{prior}})]. \quad (10)$$

In expression 10, the superscript t denotes the matrix transpose, $\mathbf{C}_\mathbf{D}$ is the a priori covariance matrix of the data, $\mathbf{C}_\mathbf{M}$ is the covariance matrix on the a priori model, $\hat{\mathbf{c}}(\mathbf{m}_n)$ is the vector representing the theoretical phase-velocities of the model $\mathbf{m}_n$, and $\mathbf{G}_n$ is the matrix of partial derivatives computed at the model $\mathbf{m}_n$:

$$(\mathbf{G}_\mathbf{n})_\alpha^i = \left(\frac{\partial \hat{c}^i}{\partial m^\alpha}\right)_{m_n}, \quad (11)$$

where $\hat{c}^i$ is the predicted phase velocity for the datum i and m^α is the value of V_S in the α layer of $\mathbf{m}_n$.

In what follows, $\mathbf{C}_\mathbf{D}$ and $\mathbf{C}_\mathbf{M}$ are diagonal (errors are considered independent). To evaluate the a priori error on the data (i.e., the square root of the diagonal elements of $\mathbf{C}_\mathbf{D}$), we use the rms deviation of phase velocities inferred from synthetic U-c diagrams (e.g., rms values on Figure 3). These values correspond to minimum measurement errors (we do not account for potentially larger errors from noise in the records), so we fix the error in the phase-velocity estimates to a larger value of 30 m/s. The a priori errors on model parameters are fixed to 40% of the a priori shear velocities in $\mathbf{m}_{\text{prior}}$. This rough estimate is based on a comparison between output of pre-

Figure 5. Inversion results from the phase velocities measured on synthetic U-c diagrams. The synthetic data are computed for (a, b) model A and (c, d) model B. In (a) and (c), inversions are based on an a priori model fixed from converting c into V_S using equation 7; in (b) and (d), inversions are based on an a priori model taken in a model library made of 5000 models and giving the best fit to the phase and group velocities. (Top) The V_S profiles corresponding to the exact model (solid black line), the inverted model (solid gray line), and the a priori model (dotted black line). (Middle) Resolution matrix (color bar is specified to the right). (Bottom) The rms data misfit at each iteration.
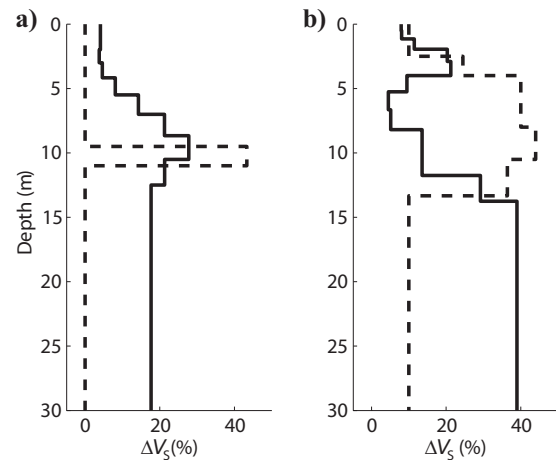

Figure 6. The V_S deviations between the preinversion outputs and (a) model A and (b) model B (see Figure 5 and Table 1). Correct inversion would predict a zero deviation. Solid lines correspond to the conversion of c into V_S, and dotted lines correspond to the model extracted from the model library.

inversion analyses and the exact models used in synthetic tests (e.g., Figure 6 for models A and B).

The inversion thus starts from an a priori model and ends when the data misfit falls below an acceptance level of 2%. Figure 5 depicts the inversion results from phase velocities measured on the *U-c* diagrams of synthetic data computed from models A and B (Table 1). Inverted V_S profiles are fairly close to the exact models, and the results do not seem to depend on the method used to establish the a priori model. Moreover, in Figure 7, we observe a good fit between the observed and predicted phase velocities. However, a low-velocity layer appears on the inverted profiles of Figure 5a and b at about 4-7-m depth. This artifact may be caused by the strong velocity contrast at 10-m depth. This bias is more visible on Figure 5a than on Figure 5b, which we could explain by the higher accuracy of the a priori model extracted from the model library in the preinversion step.

In a synthetic test, it is easy to measure how close the inverted model is from the exact one. Of course, this is not true when using actual records, and in such a case we can look at the resolution matrix **R** for a quantitative estimate of the inverted model accuracy and reliability. The resolution matrix satisfies

$$(\tilde{\mathbf{m}} - \mathbf{m}_{\text{prior}}) = \mathbf{R}(\mathbf{m}_{\text{exact}} - \mathbf{m}_{\text{prior}}), \qquad (12)$$

where $\tilde{\mathbf{m}}$ is the inverted model and $\mathbf{m}_{\text{exact}}$ is the exact model. The closer **R** is to the identity matrix, the better the resolution on the model parameter. We can write **R** as (Tarantola, 2005)

$$\mathbf{R} = \mathbf{C_M G}^t (\mathbf{G C_M G}^t + \mathbf{C_D})^{-1} \mathbf{G}, \qquad (13)$$

where **G** is the matrix of partial derivatives taken at the convergence point. Note that **R** is informative only for the second step of the inversion based on the quasi-Newton inversion scheme.

Resolution matrices shown in Figure 5a and b demonstrate that the subsurface model appears to be well resolved except in the shal-
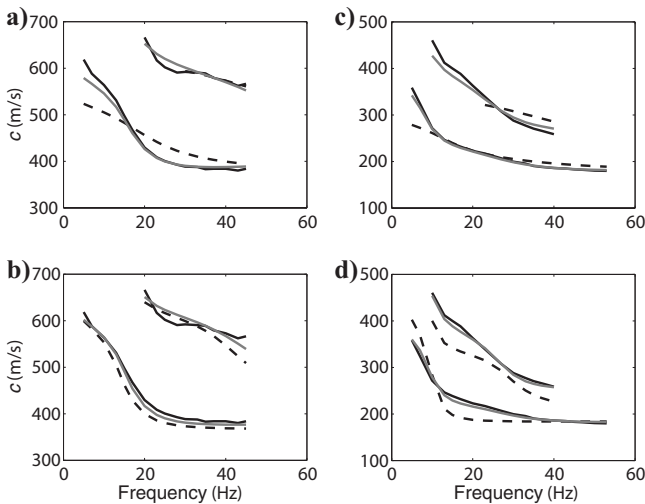
lowest layers of model A, which show a low resolution and a broader shape around the diagonal of **R**. This low resolution can be explained by the lack of high-frequency measurements in our data set, and it yields abnormally high shear velocities in the inverted model at shallow depths.

APPLICATION TO FIELD DATA

The data used to test the method were acquired on a site where seismic refraction profiles show a simple 1D structure. The field measurements were performed in September 2007 near the town of Riedseltz in Alsace, France (Figure 8). The wavefield was generated by a sledgehammer source and recorded by a linear array of 24 vertical geophones (natural frequency = 4.5 Hz). The geophone interval was 2 m, and the source offset was chosen to be 12 m to avoid the near-field effects. In Figure 8, we see that the raw data contain a strong ground roll component, and we can anticipate good-quality measurements. The largest offset trace is rejected because of its low signal-to-noise ratio.

Dispersion curves related to the records displayed in Figure 8 are estimated by using the *U-c* diagram technique, with U_c set to 250 m/s. Figure 9 displays the raw data in the *f-c* domain and shows the *U-c* diagram computed at 20 Hz. Only the fundamental mode and the first overtone are well excited at this frequency, as predicted by the previous analysis made on synthetic data.

The phase velocities inferred from the analysis of the *U-c* diagrams computed at frequencies between 9 and 60 Hz are then inverted. We use the a priori model derived from the phase-velocity conversion and the model library to start the quasi-Newton inversion. The inverted models are displayed in Figure 10; a comparison between the observed and calculated phase velocities is shown on Figure 11.

The a priori models resulting from the two preinversion procedures are quite different (see dotted lines on Figure 10a). The empirical conversion technique provides initial V_S values that are close to the final ones for intermediate depths. The same observation can be made for the model library at small and large depths.

Even if the two initial models differ, the final inverted models are remarkably similar (see solid lines on Figure 10a). In other words, the inversion converges to the same minimum of $S(\mathbf{m})$ in equation 9 even while using different starting points $\mathbf{m}_{\text{prior}}$. This does not help us determine the best preinversion strategy, but it emphasizes the robustness of the solution. This is further emphasized by the resolution matrices

Figure 7. Comparison of phase velocities inferred from the *U-c* diagrams (solid black line), the inverted model (solid gray line), and the a priori model (dotted black line). Views (a–d) correspond to (a–d) in Figure 5.
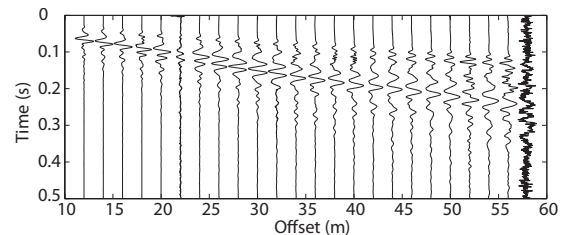

Figure 8. The shot gather obtained in Riedseltz, Alsace (France), by using a sledgehammer as the energy source. Traces are normalized by their maximum amplitudes.
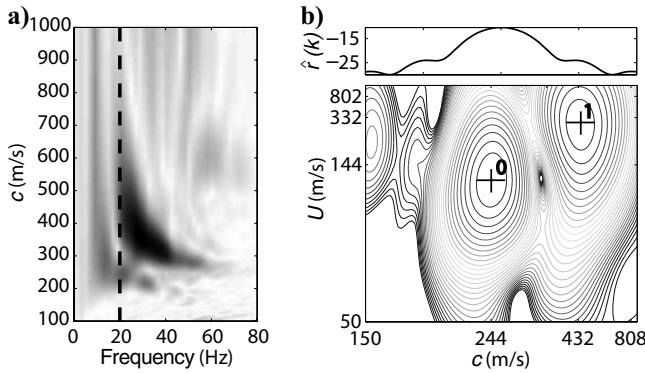
Figure 9. The *f-c* and *U-c* diagrams obtained by stacking the records shown in Figure 8. (a) The vertical dotted black line at 20 Hz on the *f-c* diagram shows the frequency at which (b) the *U-c* diagram is computed. Refer to Figure 2. The modulus of the array response is shown above the *U-c* diagram. Crosses indicate the measured group and phase-velocity values for the fundamental mode (0) and the first overtone (1).
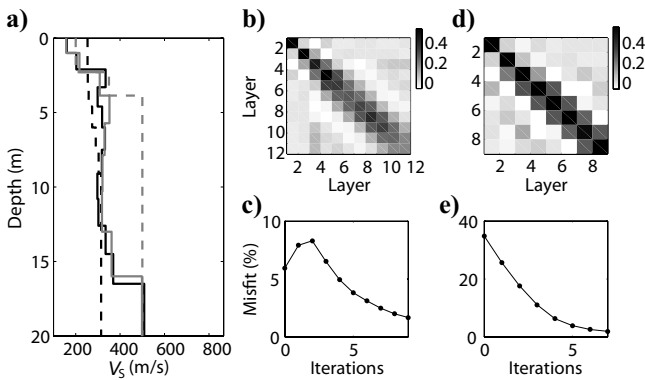

Figure 10. Inversion results from the phase-velocities measured on synthetic *U-c* diagrams. In (a), the inverted models are presented with solid lines; dotted lines depict the a priori models. Black lines correspond to inversions based on the a priori conversion of *c* into V_S associated with the resolution matrix in (b) and the data misfit in (c). Gray lines correspond to use of a model library (as for Figure 5). (d) Corresponding resolution matrix; (e) data misfit.
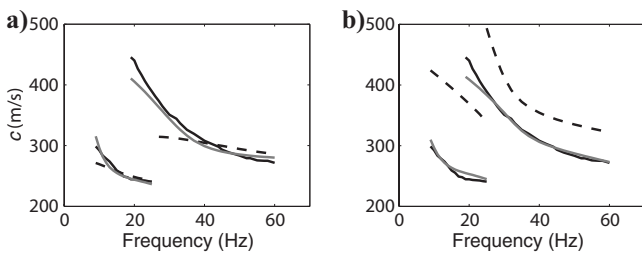

Figure 11. Comparison of phase velocities measured on the *U-c* diagrams (solid black lines) or predicted from the inverted model (solid gray lines) and the a priori model (dotted black lines). (a) Inversion based on an a priori model built from converting *c* into V_S. (b) Inversion based on the a priori model library.

Table 3. Interpretation of the inverted shear-velocity profiles displayed in Figure 10. The value *e* denotes the layer thickness; $\langle V_S \rangle$ is the average shear-velocity in each layer. The test site is located in a Pliocene basin situated in the Rhinegraben. The lithology can be observed directly on a quarry next to the seismic profile used in this study.

Lithology	*e* (m)	$\langle V_S \rangle$ (m/s)
Undifferentiated loess (Wurm age)	2.20	178
Pliocene sands	14.14	330
Oligocene marls	∞	507

R, which show a good overall resolution — particularly for the inversion based on the model-library approach.

At first sight, three well-differentiated layers can be distinguished on Figure 10. The uppermost layer, $V_S \approx 178$ m/s, corresponds to the local soil structure. This is in good agreement with the results of the P-wave refraction tomography related to the same profile (Herquel et al., 2007), which reveals a shallow 2–2.5-m-thick layer corresponding to $V_P \approx 380$ m/s overlying deeper terrains of higher velocities, $V_P \approx 620$ m/s. This 620-m/s P-wave velocity may be associated with the $V_S \approx 380$-m/s layer.

Lack of resolution of the P-wave refraction data prevents any detection of higher velocities at greater depth along this seismic profile. A larger offset would be required to observe second refracted waves. However, seismic reflections from other profiles located at a quarry cliff 1 km away from the site revealed horizons at depths comprised between 13 and 18 m (Bano et al., 2002), which could fit well with the 16.34-m depth of the last interface of our inverted V_s model. The three layers shown in Figure 10 may thus be confidently related to the lithology observed in the nearby quarry (Table 3).

CONCLUSIONS

Results obtained from synthetic and actual records show that, in addition to the fundamental mode, only the first-higher mode is observable for a point source located at the ground surface with soft soil conditions. Our examples show that the discrimination between the fundamental and the well-excited first-higher mode is clearly made easier by using *U-c* diagrams instead of classical *f-k* analysis. The high-quality dispersion data thus obtained can be processed to infer the near-surface shear velocity structure with better depth resolution than when using fundamental-mode dispersion only.

To take into account the nonlinearity in the relation between the 1D structure of the ground and the surface-wave dispersion, particularly when group velocities are involved, we have developed a two-step inversion procedure. In the first step, a preliminary inversion gives us a model used as a prior model for starting a quasi-Newton inversion in the second step. Two approaches are followed to determine this prior model: (1) conversion of the fundamental-mode phase velocity, providing a smooth a priori model, and (2) use of a model library, allowing more contrasted 1D layered models. This second method is more time consuming, but it is easily tractable on modern PCs (extraction of the a priori information from a model library of 5000 models usually takes less than 1 s on an Intel Pentium M 1.7-GHz processor). Furthermore, we may use the group-velocity information in a flexible way during this nonlinear, Monte Carlo pre-

inversion. Compared to the empirical conversion of phase velocity, the second technique provides better estimates of the 1D shear-wave profile at great depths and for highly contrasted structures.

The quasi-Newton technique applied in the second step converges rapidly to acceptable solutions for synthetic and actual data. The fact that the inverted V_S profiles depend weakly on the a priori model gives us confidence in the robustness of the solutions. A full integration of group velocities in a joint inversion process could permit a better determination of the soil structure, but it would need a more time-consuming Monte-Carlo method, which is not adapted to current field computers used for geotechnical investigations.

Finally, let us again stress the fact that the source-receiver configuration and the test area that we consider in this paper correspond to a inexpensive, classical experiment in near-surface prospecting based on surface waves (surficial source with a sledgehammer, 24 geophones, deployed on a 58-m-long linear array). This configuration limits the higher-mode content in the observed surface-wave signals. If higher-rank modes were more excited, we could have measured their dispersion and better constraints could be put on the shear velocities at large depth. The relative importance of the different modes depends on soil stratification, frequency, and depth and nature of the seismic source. A surface source such as the one we use here cannot strongly excite higher modes in soft-soil conditions. A simple but more expensive configuration to increase the resolution of the method at depth could, for example, consist of using a buried source instead of a surficial one.

ACKNOWLEDGMENTS

REFERENCES

Abbiss, C. P., 1981, Shear wave measurements of the elasticity of the ground: Geotechnique, **31**, 91–104.

Bano, M., J. Edel, G. Herquel, and Ecole et Observatoire des Sciences de la Terre (EOST) Class of 2001–2002, 2002, Geophysical investigation of a recent shallow fault: The Leading Edge, **21**, 648–650.

Beaty, K. S., D. R. Schmitt, and M. Sacchi, 2002, Simulated annealing inversion of multimode Rayleigh wave dispersion curves for geological structure: Geophysical Journal International, **151**, 622–631.

Cara, M., 1976, Observation d'ondes S_a de type SH: Pure and Applied Geophysics, **114**, 141–157.

Cara, M., and B. Minster, 1981, Multimode-analysis of Rayleigh-type L_g — Part 2, Application to southern California and the northwestern Sierra Nevada: Bulletin of the Seismological Society of America, **71**, 985–1002.

Feng, S., T. Sugiyama, and H. Yamanaka, 2005, Effectiveness of multi-mode surface wave inversion in shallow engineering site investigations: Exploration Geophysics, **32**, 26–33.

Forbriger, T., 2003, Inversion of shallow-seismic wavefields: I. Wavefield transformation: Geophysical Journal International, **153**, 719–734.

Gabriels, P., R. Snieder, and G. Nolet, 1987, In situ measurements of shear-wave velocity in sediments with higher-mode Rayleigh waves: Geophysical Prospecting, **35**, 187–196.

Herquel, G., J. Edel, M. Bano, and Ecole et Observatoire des Sciences de la Terre (EOST) Class of 2007–2008, 2007, Riedseltz final report: Université de Strasbourg.

Herrmann, R. B., 2006, Computer programs in seismology — User's manual, ftp://ftp.eas.slu.edu/pub/rbh/TUTORIAL.330/cps330o.pdf, accessed 21 January 2010.

Kovach, R. L., 1965, Seismic surface waves: Some observations and recent developments: Physics and Chemistry of the Earth, **6**, 251–314.

Luo, Y., J. Xia, J. Liu, Q. Liu, and S. Xu, 2007, Joint inversion of high-frequency surface waves with fundamental and higher modes: Journal of Applied Geophysics, **62**, 375–384.

Luo, Y., J. Xia, R. D. Miller, Y. Xu, J. Liu, and Q. Liu, 2008, Rayleigh-wave dispersive energy imaging using a high-resolution linear Radon transform: Pure and Applied Geophysics, **165**, 903–922.

Mari, J. L., 1984, Estimation of static corrections for shear-wave profiling using the dispersion properties of Love waves: Geophysics, **49**, 1169–1179.

McMechan, G. A., and M. J. Yedlin, 1981, Analysis of dispersive waves by wave field transformation: Geophysics, **46**, 869–874.

Merrer, S., M. Cara, L. Rivera, and J. Ritsema, 2007, Upper mantle structure beneath continents: New constraints from multi-mode Rayleigh wave data in western North America and southern Africa: Geophysical Research Letters, **34**, L06309.

Nolet, G., 1975, Higher Rayleigh modes in western Europe: Geophysical Research Letters, **2**, 60–62.

Oliver, J., and M. Ewing, 1957, Higher modes of continental Rayleigh waves: Bulletin of the Seismological Society of America, **47**, 187–204.

O'Neil, A., T. Campbell, and T. Matsuoka, 2008, Lateral resolution and lithological interpretation of surface wave profiling: The Leading Edge, **27**, 1550–1563.

O'Neil, A., and T. Matsuoka, 2005, Dominant higher surface-wave modes and possible inversion pitfalls: Journal of Environmental and Engineering Geophysics, **10**, 185–201.

Park, C. B., R. D. Miller, and J. Xia, 1999, Multichannel analysis of surface waves: Geophysics, **64**, 800–808.

Socco, L. V., and C. Strobbia, 2004, Surface-wave method for near-surface characterization — A tutorial: Near Surface Geophysics, **2**, 165–185.

Song, Y. Y., J. P. Castagna, R. A. Black, and R. W. Knapp, 1989, Sensitivity of near-surface shear-wave velocity determination from Rayleigh and Love waves: 59th Annual International Meeting, SEG, Expanded Abstracts, 509–512.

Tarantola, A., 2005, Inverse problem theory and methods for model parameter estimation: SIAM.

Xia, J., R. D. Miller, and C. B. Park, 1999, Estimation of near-surface shear-wave velocity by inversion of Rayleigh waves: Geophysics, **64**, 691–700.

Xia, J., R. D. Miller, C. B. Park, and G. Tian, 2003, Inversion of high frequency surface waves with fundamental and higher modes: Journal of Applied Geophysics, **52**, 45–57.